

Warming the early Earth - CO₂ reconsidered

Philip von Paris ^{a,*}, Heike Rauer ^{a,b}, J. Lee Grenfell ^{a,b},
Beate Patzer ^b, Pascal Hedelt ^a, Barbara Stracke ^a,
Thomas Trautmann ^c and Franz Schreier ^c

^a*Institut für Planetenforschung, Deutsches Zentrum für Luft- und Raumfahrt,
Rutherfordstr. 2, 12489 Berlin (Germany)*

^b*Zentrum für Astronomie & Astrophysik, Technische Universität Berlin,
Hardenbergstr. 36, 10623 Berlin, (Germany)*

^c*Institut für Methodik der Fernerkundung, Deutsches Zentrum für Luft- und
Raumfahrt, Münchener Str. 20, 82234 Wessling (Germany)*

Abstract

Despite a fainter Sun, the surface of the early Earth was mostly ice-free. Proposed solutions to this so-called "faint young Sun problem" have usually involved higher amounts of greenhouse gases than present in the modern-day atmosphere. However, geological evidence seemed to indicate that the atmospheric CO₂ concentrations during the Archaean and Proterozoic were far too low to keep the surface from freezing. With a radiative-convective model including new, updated thermal absorption coefficients, we found that the amount of CO₂ necessary to obtain 273 K at the surface is reduced up to an order of magnitude compared to previous studies. For the late Archaean and early Proterozoic period of the Earth, we calculate that CO₂ partial pressures of only about 2.9 mb are required to keep its surface from freezing which is compatible with the amount inferred from sediment studies. This conclusion was not significantly changed when we varied model parameters such as relative humidity or surface albedo, obtaining CO₂ partial pressures for the late Archaean between 1.5 and 5.5 mb. Thus, the contradiction between sediment data

and model results disappears for the late Archaean and early Proterozoic.

Key words:

Faint Young Sun problem, Earth - Atmospheres, composition - Radiative transfer

1 Introduction

Geological evidence has shown that liquid water was present on the Earth's surface earlier than 3.7 Gy ago (e.g., Mojzsis et al., 1996; Rosing and Frei, 2004) which implies average temperatures on the surface above 273 K. Some authors have even argued for a hot Archaean climate ($T > 340$ K), based on oxygen (Knauth and Lowe, 2003) and silicon (Robert and Chaussidon, 2006) isotope analysis of seawater cherts. However, as pointed out by, e.g., Kasting and Howard (2006) and Shields and Kasting (2007), these isotopic signatures changes might not only be caused by temperature effects. Sleep and Hessler (2006), for example, deduced a more moderate surface temperature below 300 K, based on quartz weathering records in paleosols. Nevertheless, it is generally accepted that the Earth has been ice-free throughout most of its history.

Observations of several solar-type stars of different ages and virtually all standard models of the solar interior have shown that the total solar luminosity has increased since the ZAMS (Zero Age Main Sequence) by about 30% (Gough, 1981; Caldeira and Kasting, 1992). Had the composition of the Earth's atmosphere been the same then as today, the reduced solar flux would have resulted in surface temperatures below 273 K prior to 2.0 Gy (Sagan and Mullen, 1972). This apparent contradiction between solar evolution models, climatic simulations and geological evidence for liquid water and moderately warm temperatures on Earth has been termed the "faint young Sun problem".

Numerous studies have attempted to solve this problem. For example, Minton and Malhotra

* Corresponding author: philip.vonparis@dlr.de

(2007) explored the hot early Sun scenario for a non-standard solar evolution. Shaviv (2003) showed that moderate greenhouse warming in combination with the influence of solar wind and cosmic rays on climate could resolve the problem. Jenkins (2000) assumed high obliquities in a General Circulation Model to account for high Archaean temperatures.

However, the most accepted scenario involves a much enhanced greenhouse effect (GHE) on the early Earth compared to modern Earth. Today, the GHE produces around 30 K of warming, raising the mean surface temperature of the Earth to about 288 K. Increased abundances of greenhouse gases such as carbon dioxide (Kasting, 1987), methane (Pavlov et al., 2000), ethane (Haqq-Misra et al., 2008) or ammonia (Sagan and Mullen, 1972; Sagan and Chyba, 1997) will strengthen the GHE, hence potentially resolve the problem. However, all of these studies faced some form of contradictions or large uncertainties, either from geological data on atmospheric conditions or from atmospheric modeling. The formation and destruction of ammonia is highly dependent on UV levels in the atmosphere (Sagan and Chyba, 1997; Pavlov et al., 2001). The hydrocarbon haze necessary to allow higher hydrocarbons to accumulate in the atmosphere depends critically on the CO_2/CH_4 ratio (Pavlov et al., 2003). The high values of methane required to heat the surface of the early Earth depend on estimates of the early biosphere and volcanic activity, which is not well determined. Past CO_2 concentrations required by atmospheric models (Kasting, 1987) to reach surface temperatures above 273 K are in conflict with inferred concentrations from the sediment data (Hessler et al., 2004; Rye et al., 1995).

In this work, the role of CO_2 in warming the early Earth is reconsidered. We used a one-dimensional radiative-convective model, including updated absorption coefficients in its radiation scheme for thermal radiation. The model was applied to the atmosphere of the early Earth in order to investigate the effect of enhanced carbon dioxide on its climate. Additionally, we investigated the effect of two important parameters, namely the surface albedo and the relative

52 humidity, upon the resulting surface temperature.

53 Our results imply that the amount of CO₂ needed to warm the surface of early
54 Earth might have been over-estimated by previous studies. Furthermore, the
55 results show that the contradiction between modelled CO₂ concentrations and
56 measured values might disappear by the end of the Archaean.

57 Section 2 describes the model and section 3 the runs to validate the new radia-
58 tion scheme. The runs performed for this work are explained and summarized
59 in section 4. In section 5, the results are presented and discussed. Section 6
60 gives the summary of the results.

61 **2 Atmospheric Model**

62 We used a one-dimensional radiative-convective model based on the climate
63 part of the model used by Segura et al. (2003) and Grenfell et al. (2007a,b).
64 Our model differs in upgrades of the radiation scheme to calculate the thermal
65 emission in the atmosphere. The model calculates globally, diurnally-averaged
66 atmospheric temperature and water profiles for cloud-free conditions. We will
67 first state some basic characteristics of the model (2.1). Then we will describe
68 the calculation of the energy transport via radiative transfer (solar and thermal
69 fluxes) and convection (2.2) to obtain the atmospheric temperature profile.
70 Thereafter, a description of the determination of the water profile is given
71 (2.3). Finally, the model input parameters are summarized (2.4).

72 *2.1 Basic model description*

73 The model determines the temperature profile by assuming two dominant
74 mechanisms of energy transport, i.e. radiative transfer and convection. The
75 convective lapse rate is assumed to be adiabatic. The radiative lapse rate is

76 calculated from contributions of both solar and thermal radiation, including
77 Rayleigh scattering for solar radiation and continuum absorption in the ther-
78 mal region. Table 1 summarizes the contributions of the different atmospheric
79 species to the calculation of the temperature profile.

80 The species considered in the model are molecular nitrogen, water, molecular
81 oxygen, argon, carbon dioxide and carbon monoxide. For example, a typi-
82 cal early Earth run considered 0.77 bar of nitrogen and several (2.9 - 57.2)
83 mb of carbon dioxide in addition to water in varying concentrations (0.5—1
84 % at the surface). Molecular nitrogen is an effective Rayleigh scatterer (al-
85 though not as effective as carbon dioxide) and as a main constituent of the
86 atmosphere also contributes to the heat capacity. Water is not considered to
87 be an important Rayleigh scatterer, but it is relevant for the other radiative
88 processes. Also, water influences the adiabatic lapse rate because it readily
89 condenses in the troposphere. However, due to small mixing ratios, especially
90 in the stratosphere, water vapour does not contribute to the heat capacity of
91 the atmosphere. Molecular oxygen and argon do contribute to the heat capac-
92 ity of the atmosphere, and molecular oxygen additionally contributes to the
93 Rayleigh scattering coefficient. Carbon dioxide contributes to all relevant ra-
94 diative mechanisms (molecular absorption of solar and thermal radiation, con-
95 tinuum absorption, Rayleigh scattering), but not to the adiabatic lapse rate
96 because it does not condense under conditions described in this paper. Carbon
97 monoxide is an important absorber species in some mid-infrared windows and
98 contributes to the heat capacity.

99 The model assumes the hydrostatic relation between pressure p and density
100 ρ throughout the plane-parallel atmosphere. On the 52 model layers, a loga-
101 rithmic pressure grid is calculated. Specified pressure levels at the planetary
102 surface (e.g., 1 bar for the standard Earth case) and the upper model lid (at
103 $6.6 \cdot 10^{-5}$ bar) determine the altitude range which, for modern Earth conditions,
104 extends to 65-70 km, i.e. the lower- to mid mesosphere. For all gases except

105 water, the ideal gas law is taken as the equation of state (see 2.2.4 for water).
 106 The effect of clouds is difficult to incorporate into 1D models (see, for example,
 107 Pavlov et al., 2000; Segura et al., 2003). In the present model, following the
 108 approach of Segura et al. (2003), clouds are implicitly included by adjusting
 109 the surface albedo A_{surf} such that under modern Earth control conditions the
 110 model calculates a mean surface temperature of 288 K. The required value for
 111 A_{surf} is about 0.21, whereas the actual global value for Earth is approximately
 112 0.15. This can be interpreted as a ground cloud layer instead of tropospheric or
 113 stratospheric clouds. The model uses a time-stepping algorithm to convergence
 114 to the steady-state solution (Pavlov et al., 2000).

115 2.2 Temperature profile

116 During each time step, the temperature profile is calculated from the radia-
 117 tive equilibrium condition. The temperature T on an atmospheric level z is
 118 determined by the following equation of energy conservation (Pavlov et al.,
 119 2000):

$$\frac{d}{dt}T(z) = -\frac{g}{c_p(T, z)} \frac{dF(z)}{dp(z)} \quad (1)$$

120 where dt is the time step in the model, c_p the heat capacity, F the total net
 121 radiative flux and p the pressure of the level. The radiative flux F is the sum of
 122 thermal planetary and atmospheric emission, F_{thermal} , and the solar radiative
 123 input, F_{solar} , into the atmosphere:

$$F(z) = F_{\text{thermal}}(z) + F_{\text{solar}}(z) \quad (2)$$

124 These fluxes are calculated separately by two numerical schemes which solve
 125 the monochromatic radiative transfer equation (RTE) for the spectral intensity
 126 I_ν in the respective spectral domain (i.e., near-UV to near-IR for solar flux,

127 near-IR to far-IR for thermal flux):

$$\mu \frac{dI_\nu}{d\tau_\nu} = I_\nu - S_\nu \quad (3)$$

128 where S_ν is the source function (either the incident solar radiation or the ther-
 129 mal blackbody emission of the atmospheric layers and the planetary surface),
 130 $d\tau_\nu$ the optical depth and $\mu = \cos(\theta)$ the cosine of the polar angle. The optical
 131 depth is defined as usual by

$$d\tau = -(\kappa_\nu + s_\nu)dz \quad (4)$$

132 where κ_ν and s_ν represent the absorption coefficient and the scattering coef-
 133 ficient respectively. The absorption coefficient for a gas mixture is calculated
 134 from the individual absorption coefficients of the gas species i :

$$\kappa_\nu = \sum_i \kappa_{\nu,i} = \sum_i \sigma_{\text{abs},i} \cdot N_i \quad (5)$$

135 where N_i is the number density and $\sigma_{\text{abs},i}$ the molecular absorption cross section
 136 of the gas species i . When no scattering occurs (i.e., $s_\nu = 0$), eq. 4 can be
 137 written in terms of the column density W_i of the gas species i as:

$$\tau = \sum_i \sigma_{\text{abs},i} \cdot W_i \quad (6)$$

138 The absorption cross section is defined by:

$$\sigma_{\text{abs}}(\nu, p, T) = \sum_j S_j(T) \cdot g_j(\nu, T, p) \quad (7)$$

139 Here, $S_j(T)$ is the temperature-dependent line strength of a particular spec-
 140 tral line j and $g_j(\nu, T, p)$ the temperature- and pressure-dependent line shape

141 function of the same line.

142 For the scattering coefficient, an analogous equation is valid:

$$s_\nu = \sum_i s_{\nu,i} = \sum_i \sigma_{y,i}(\nu) \cdot N_i \quad (8)$$

143 Here, $\sigma_{y,i}(\nu)$ is a scattering cross section of type y . In the present model,
144 Rayleigh scattering is considered.

145 The solution of eq. (4), i.e. the calculation of optical depths, is one of the key
146 elements in radiative-convective models. This solution, of course, depends on
147 the accurate calculation of the absorption cross sections.

148 From eq. (3), the necessary fluxes for eq. (2) (i.e., the thermal and the solar
149 flux) are obtained by an angular integration of the (monochromatic) intensity:

$$F_\nu = \int_\Omega d\omega \mu I_\nu \quad (9)$$

150 and a frequency integration of the (monochromatic) flux:

$$F_{\nu_1 \rightarrow \nu_2} = \int_{\nu_1}^{\nu_2} F_\nu d\nu \quad (10)$$

151 Each one of these integrations is performed independently for the two compo-
152 nents of the total flux.

153 2.2.1 Solar radiation

154 The solar radiation module which calculates $F_{\text{solar}}(z)$ for eq. (2) has already
155 been used by, e.g., Pavlov et al. (2000); Segura et al. (2003) or Grenfell et al.
156 (2007a) and is based on Kasting et al. (1984b) and Kasting (1988). The module
157 considers a spectral range from 0.26 to 4.5 μm in 38 intervals. It evaluates the

158 solar incident radiation at a fixed daytime average solar zenith angle of 60° .
 159 Contributions to the optical depth come from gaseous absorption by water
 160 and carbon dioxide (i.e., κ_ν in eq. (4)) and from Rayleigh scattering by carbon
 161 dioxide, molecular nitrogen and molecular oxygen (i.e., s_ν in eq. (4)).

162 Absorption cross sections σ_{abs} for the solar code were obtained from the HI-
 163 TRAN 1992 database (Rothman et al., 1992). Rayleigh scattering cross sec-
 164 tions σ_{ray} are parameterized following Vardavas and Carver (1984). The fre-
 165 quency integration (see also eq. (10)) of the RTE for F_{solar} in each of the 38
 166 spectral intervals is parameterized by a four-term correlated-k exponential sum
 167 (e.g., Wiscombe and Evans, 1977). The following angular integration (eq. (9))
 168 is performed by using a quadrature δ -2-stream approximation code based on
 169 Toon et al. (1989). The resulting fluxes from each spectral interval are added
 170 up to yield the total solar flux $F_{\text{solar}}(z)$ at an atmospheric level z . This flux is
 171 further multiplied by a factor of 0.5 to account for diurnal variation.

172 2.2.2 Thermal molecular absorption

173 The thermal (planetary) radiation module for $F_{\text{thermal}}(z)$ in eq. (2) consid-
 174 ers a spectral range from 1 to $500 \mu\text{m}$ in 25 intervals. Our new thermal
 175 module is called MRAC (Modified RRTM for Application in CO_2 -dominated
 176 Atmospheres) and is based on the radiation scheme RRTM (Rapid Radia-
 177 tive Transfer Model). RRTM was developed by Mlawer et al. (1997) and has
 178 been used by numerous other modeling studies (e.g., Segura et al., 2003, 2005;
 179 Grenfell et al., 2007a,b). The need for a new radiation model comes from the
 180 fact that RRTM was specifically designed for conditions of modern Earth, i.e.
 181 it is not adaptable to studies of atmospheres which greatly differ from mod-
 182 ern atmospheric conditions (in terms of atmospheric composition, temperature
 183 structure, pressure, etc.). MRAC is easily adaptable to varying conditions, as
 184 is described below.

185 MRAC uses the correlated- k approach (e.g., Goody et al., 1989; Lacis and Oinas,

1991; Colaprete and Toon, 2003) for the frequency integration of the RTE in the thermal range, as does RRTM. The planetary surface (bottom layer of the model atmosphere) and the atmospheric layers are taken as blackbody emitters, according to their respective temperatures. The thermal surface emissivity is set to unity. The absorber species considered in MRAC are water, carbon dioxide and carbon monoxide. The angular integration (eq. (9)) is performed using the diffusivity approximation (as in Mlawer et al., 1997).

193 *The correlated- k method*

Basically, this method transfers the frequency integration (FI) of the RTE from frequency space ν to a probability space g . For the absorption cross section σ_{abs} of eq. (7) in an interval $[\nu_1, \nu_2]$, a probabilistic density distribution $f(\sigma_{\text{abs}})$ (i.e., probability of occurrence for a particular value of σ_{abs}) with the following normalization condition can be defined:

$$\int_0^\infty f(\sigma_{\text{abs}}) d\sigma_{\text{abs}} = 1 \quad (11)$$

To follow conventional nomenclature in the literature regarding k -distributions, σ_{abs} is hereafter referred to as k . The function $f(\sigma_{\text{abs}}) = f(k)$ is called the k -distribution. From the k -distribution, a cumulative k -distribution $g(k)$ can be defined by

$$g(k) = \int_0^k f(k') dk' \quad (12)$$

The cumulative k -distribution is a strictly monotonic function and may thus be inverted from $g(k)$ to yield $k(g)$. This mapping of the frequency information ($k(\nu)$) into a single probability variable ($k(g)$) can be done because it is irrelevant at which position of the spectral interval a particular value of the absorption cross section k occurs. Performing a variable substitution in eq. (10) then leads to the following equation:

$$F_{\nu_1 \rightarrow \nu_2} = \int_{\nu_1}^{\nu_2} F(\nu) d\nu = \int_0^1 F(g) dg \quad (13)$$

209 The goal of the cumulative- k approach is to reduce the number of radiative
 210 transfer operations drastically while keeping the accuracy of line-by-line mod-
 211 els. This can be achieved with very few numbers of points in g space (see
 212 Goody et al., 1989; West et al., 1990). The g integration in eq. (13) is per-
 213 formed in MRAC by Gaussian quadrature using 16 intervals in g space (the
 214 same as used in RRTM, Mlawer et al., 1997).

215 The extension of this exact method from homogeneous to inhomogeneous at-
 216 mospheres is called the correlated- k method (e.g., Mlawer et al., 1997). Each
 217 g interval is treated as if it were a monochromatic frequency interval, i.e. the
 218 method uses the same subset of g space for all layers throughout the atmo-
 219 sphere. This implies a full frequency correlation of a specific subset of g space
 220 for all atmospheric layers. There are conditions under which this approach is
 221 exact (Goody and Yung, 1989), but usually these do not hold. However, the
 222 numerical error of the correlated- k method is generally small (Mlawer et al.,
 223 1997).

224 *Creating the new radiation scheme*

225 MRAC was originally designed to simulate atmospheres of a wide range of pos-
 226 sible terrestrial planets other than modern Earth, as stated above. Therefore, a
 227 new temperature-pressure (T - p) grid to incorporate the aforementioned (T , p)-
 228 dependence of the absorption cross sections (see eq. 7) has been introduced.
 229 In RRTM, k values are tabulated for every spectral band and every point in g
 230 space for 59 pressure levels and the associated Mid-Latitude-Summer (MLS)
 231 standard Earth temperature values as well as temperature values $T_{\text{MLS}} \pm 15$ K
 232 and $T_{\text{MLS}} \pm 30$ K, as described in Mlawer et al. (1997). The T - p grid of RRTM
 233 is thus more or less fixed to modern Earth conditions. For MRAC, we used
 234 8 pressure levels, ranging equidistantly in $\log p$ from 10^{-5} to 100 bar and 9

temperature points, 6 in 50 K steps from 150 K to 400 K and three additional points for 500, 600, 700 K respectively. Tests showed that this grid allows for an interpolation accuracy of usually better than 2-3%. Furthermore, the number of T - p points is consistent with previous modeling studies (Kasting et al., 1993; Colaprete and Toon, 2003).

Figure 1 shows the range of the tabulated k -values for both RRTM and MRAC, i.e. the interpolation regime of the two radiative schemes. It demonstrates that RRTM can only be applied to a much narrower range of atmospheric conditions in comparison to MRAC.

The necessary re-calculation of the k -distributions for each of the gases included in MRAC (water, carbon dioxide, carbon monoxide) proceeded in three steps:

First, the absorption cross sections for every species were calculated for each T - p grid point in each of the spectral intervals where the respective species is active. The line shape cut-off was set to 10 cm^{-1} from the frequency ν , i.e. the sum over j in eq. (7) contains contributions from all lines within $\pm 10 \text{ cm}^{-1}$. For the line shape $g_j(\nu, T, p)$, a Voigt profile was assumed. The required line parameters were taken from the HiTemp 1995 database (Rothman et al., 1995). The foreign broadening parameters in HiTemp are given for air, i.e. an oxygen-nitrogen mixture as a background atmosphere. However, as reported by several authors (e.g., Brown et al., 2005; Toth, 2000), the foreign broadening parameters vary by significant amounts when different broadening gases are considered. Thus, for each type of background atmosphere, a new set of k -distributions must be generated (e.g., low-oxygen atmospheres, CO_2 -dominated atmospheres, intermediate N_2 - O_2 -atmospheres). These line parameters were then used as input to a line-by-line radiative transfer model called Mirart (Schreier and Böttger, 2003). Mirart produced the actual absorption cross sections with a spectral resolution of 10^6 equidistant points per spectral interval.

Second, the k -distributions $f(k)$ were calculated from the absorption cross

sections. From the k distribution $f(k)$, the cumulative k -distribution $g(k)$ was then obtained.

Third, representative k values were calculated for each of the g subintervals. In this step, our algorithm followed the approach of Mlawer et al. (1997), i.e. for each of the 16 Gaussian subintervals in g space, an arithmetic mean absorption cross section was calculated.

MRAC also implements a so-called binary species parameter η for transmittance calculations. This is employed in intervals having two important absorber species (for more details, see Mlawer et al., 1997 or Colaprete and Toon, 2003):

$$\eta = \frac{C_1}{C_1 + r \cdot C_2} \quad (14)$$

Here, $C_{1,2}$ are the concentrations of the two gases (in the case of MRAC, water and carbon dioxide) and r is some specified reference ratio (mean modern Earth tropospheric values). Carbon monoxide, although present in the model in six spectral intervals, is not considered to be part of the binary species parameter. This is partly due to the expected low concentrations in the simulated atmospheres (typical theoretical and measured values for early Earth and Mars are below 10^{-4} volume mixing ratio), partly due to the expected low temperatures (below 300 K), which means that the strong CO fundamentals around $4 \mu\text{m}$ are completely outside the relevant Planck emission windows. Consequently, carbon monoxide has only a reduced impact on the radiation budget, compared to water and carbon dioxide. k -distributions are calculated in MRAC for 5 different values of η , ranging equidistantly from 0 (CO₂ only) to 1 (H₂O only).

Another improvement in MRAC, compared to RRTM, is the treatment of the Planck function in each band. The fraction of thermal radiance associated with a subset in g space is calculated from eq. (11) in Mlawer et al. (1997):

$$f_g = \frac{B_g w_g}{\overline{B}_g} \quad (15)$$

Here, B_g is the average Planck function of the frequencies in the subset of g space, w_g the Gaussian weight of the g interval and \overline{B}_g the average Planck function of the whole spectral band (i.e., the whole g space). As temperature, pressure and species concentrations vary, the different g subsets will correspond to different frequencies, and as such the value of B_g , thus f_g , will vary. This has been taken into account while constructing the k -distributions.

Mlawer et al. (1997) tabulated values of f_g for every value of the binary species parameter and for two atmospheric reference levels, one each in the troposphere and the stratosphere. In MRAC, values of f_g were tabulated for three temperatures and two pressure levels as well as for the values of the binary species parameter. The most important factor for f_g is the binary species parameter η , whereas the variation with temperature and pressure is rather small, although not negligible. Therefore these 6 T - p points are regarded as to be sufficient.

A further difference between RRTM and MRAC is the distinction between troposphere and stratosphere. In the troposphere, RRTM changes major and minor absorbers in some of the spectral intervals (see table 1 in Mlawer et al., 1997). In some spectral bands, no absorption is considered in the stratosphere, in others, the number of key species is reduced. This is done because on Earth, the chemical and physical regimes are quite different in the troposphere compared to those in the stratosphere. However, as this is mostly due to Earth-specific conditions (e.g., the cold trap, tropopause and temperature inversion all approximately occur at the same altitude), this distinction was not incorporated into MRAC.

312 2.2.3 Thermal continuum absorption

313 Based on approximation formulations used by Kasting et al. (1984b), Kasting et al.
 314 (1984a) and Colaprete and Toon (2003), additional CO₂ and H₂O continuum
 315 absorption in the thermal region is considered. In contrast, the RRTM scheme
 316 only considers water continuum absorption (Mlawer et al., 1997).

317 Equation (16) shows the approximation for the optical depth $\tau_{\text{cont,CO}_2}$ due
 318 to CO₂ continuum absorption. The corresponding parameters are taken from
 319 Kasting et al. (1984b).

$$\tau_{\text{cont,CO}_2} = C_i W \cdot p_E \left(\frac{T_0}{T} \right)^{t_i} \quad (16)$$

320 In this equation, C_i a frequency-dependent adjustment to the path length,
 321 W the column amount of CO₂, $p_E = (1 + 0.3 \cdot C_{\text{CO}_2}) \cdot p$ (p layer pressure,
 322 C_{CO_2} concentration) an effective CO₂ broadening pressure and $T_0=300$ K is a
 323 reference temperature.

324 The optical depth $\tau_{\text{cont,H}_2\text{O}}$ due to water continuum absorption in the window
 325 region (8-12 μm) is calculated from the equation (Kasting et al., 1984a)

$$\tau_{\text{cont,H}_2\text{O}} = h_n \cdot p \cdot \frac{W_w^2}{W_t} \quad (17)$$

326 where $h_n = h_t \cdot h_\nu$ incorporates the frequency and temperature dependence, p is
 327 the pressure, W_t the total and W_w the water column of the layer. h_ν is evaluated
 328 at the high frequency interval boundary, as in Kasting et al. (1984a). We use
 329 the following approximations for h_t and h_ν , based on Kasting et al. (1984a)
 330 and Colaprete and Toon (2003):

$$h_t = e^{1800 \cdot (\frac{1}{T} - \frac{1}{296})} \quad (18)$$

$$h_\nu = 1.25 \cdot 10^{-22} + 1.67 \cdot 10^{-19} \cdot e^{-2.62 \cdot 10^{-13} \cdot \nu} \quad (19)$$

Both the water and the carbon dioxide continuum absorption are considered to be approximately monochromatic over a specific spectral interval, hence their contribution to the overall absorption coefficient (see eq. (4)) is added as a constant term.

2.2.4 Convective adjustment

Convective adjustment to the lapse rate is performed whenever the calculated radiative lapse rate $\nabla_{\text{rad}}T$ exceeds the adiabatic value $\nabla_{\text{ad}}T$ (Schwarzschild criterion):

$$\nabla_{\text{rad}}T > \nabla_{\text{ad}}T \quad (20)$$

The adiabatic lapse rate is calculated as a standard dry adiabat in the stratosphere. In the troposphere, a wet H₂O adiabatic lapse rate is assumed. Below 273 K, the Clausius-Clapeyron-equation $\frac{d \ln(p_v)}{d \ln(T)} = \frac{m \cdot L}{R \cdot T}$ (R universal gas constant, m mass, L latent heat release per mass) for the saturation vapor pressure curve p_v is applied. Between 273 and 647 K, a formulation by Ingersoll (1969) is taken.

2.3 Atmospheric water profile

In every time step, the water vapor profile is re-calculated according to the new temperature profile.

In the troposphere, water vapor concentrations $C_{\text{H}_2\text{O}}$ are calculated from a fixed relative humidity distribution RH :

$$C_{\text{H}_2\text{O}}(T, z) = \frac{p_{\text{sat}}(T(z))}{p(z)} \cdot RH(z) \quad (21)$$

where p_{sat} is the saturation vapor pressure of water at the given temperature T and p the atmospheric pressure at level z . The default relative humidity profile RH follows the approach of Manabe and Wetherald (1967), with a relative humidity R_s of 80% at the surface.

$$RH(z) = R_s \cdot \frac{\frac{p(z)}{p_{\text{surface}}} - 0.02}{0.98} \quad (22)$$

Above the cold trap, water vapor is treated as a non-condensable gas, and its concentration is fixed at the cold trap value.

2.4 Boundary conditions, initial values and parameters

Since eq. (1) is a first order differential equation for the temperature, a starting temperature profile must be provided. In addition, a boundary condition for the radiative flux must be specified. To obtain unique equilibrium solutions, parameters must also be provided for the model. These include pressure parameters for the planetary top-of-atmosphere (TOA) pressure p_0 , gas concentrations, surface albedo or solar zenith angle, for example.

Table 2 summarizes the boundary conditions, initial values and parameters.

3 Validation of the new radiation scheme

3.1 General remarks

MRAC has been tested in two different ways.

367 • Case 1: k -distributions

368 The calculated k -distributions, i.e. the model input data, have been val-
369 idated against published values to show that the algorithm creating the
370 k -distributions works correctly.

371 • Case 2: Earth atmosphere temperature profiles

372 Temperature profiles of an Earth-like test atmospheres (composition: N₂
373 0.77, O₂ 0.21, Ar 0.01, CO₂ $3.55 \cdot 10^{-4}$) calculated with MRAC and RRTM
374 have been compared. This was done since RRTM has been extensively
375 validated both against line-by-line codes and atmospheric measurements
376 (Mlawer et al., 1997) under modern Earth conditions.

377 Our test atmosphere has a composition close to the present day atmo-
378 sphere. However, it lacks radiative trace gases such as nitrous oxide, ozone
379 and methane, as these gases cannot be handled by MRAC yet (see above).
380 Note that due to the lack of ozone in our test atmosphere, we do not expect
381 a large stratospheric temperature maximum as is observed in the present
382 Earth atmosphere because this maximum is almost entirely due to the ab-
383 sorption of solar radiation by ozone.

384 We additionally performed test runs on a second test atmosphere (not
385 shown) which differs from the first one by its CO₂ content (100-fold increase).
386 This 100-fold increase in CO₂ represents the current limit for the RRTM
387 scheme (Segura et al., 2003, Eli Mlawer, priv. comm.).

388 These two validation approaches are discussed below.

389 3.2 k -distributions

390 Figures 2 and 3 compare our calculated k -distributions (dotted lines) with
391 previously published values (plain lines) for different water and carbon dioxide
392 bands. Published values were taken from Lacis and Oinas (1991) (H₂O, Fig.
393 2) and Mlawer et al. (1997) (CO₂, Fig. 3). Figures 2 and 3 indicate quite good
394 agreement with the published values.

395 3.3 *Earth temperature profiles*

396 The calculated temperature profiles for the test atmosphere are shown in Fig.
397 4.

398 Figure 4 implies some differences in the middle to upper stratosphere (2-6 K)
399 and small deviations ($\ll 1K$) below about 20 km. For the test atmosphere
400 with a 100-fold increase in CO₂ (not shown), the stratospheric differences are
401 even larger (up to 10 K). We interpret these differences in the temperature
402 profiles as follows:

403 Firstly, as stated above in section 2.2.2, MRAC does not differentiate between
404 troposphere and stratosphere, as is the case for RRTM. That means, spectral
405 bands where H₂O or CO₂ absorb only weak are not considered for optical depth
406 calculations in the stratosphere by RRTM (e.g., bands 6, 12-13 and 15-16). In
407 contrast, MRAC incorporates the contribution of CO₂ and H₂O to the optical
408 depth in these spectral bands. However, this contribution is usually rather
409 small.

410 Secondly, and more importantly, the differences between the stratospheric tem-
411 perature profiles occur where RRTM has to use a temperature extrapolation
412 for the absorption cross sections beyond the limits of its tabulated values.

413 Fig. 5, shows the temperature profile for our test atmosphere Earth 1. Also
414 shown is the validity range of RRTM as already indicated in Fig. 1. This rep-
415 resents the lower temperature limit for the tabulated absorption cross sections
416 in RRTM, as stated above.

417 As can be seen from Fig. 5, the calculated temperature values for the first test
418 atmosphere are below the lower RRTM validity limit. Therefore, RRTM uses
419 linear extrapolation to calculate the absorption cross sections. This introduces
420 a large extrapolation error. On average, the calculated absorption cross sec-
421 tions are a factor of 2-5 too low, depending on the spectral band. Sometimes,

422 the extrapolation performed by RRTM even yields negative absorption cross
 423 sections. The interpolation errors in MRAC, on the contrary, reach only 1-2%
 424 on average.

425 Figure 6 shows the radiative fluxes and heating and cooling rates calculated by
 426 RRTM and MRAC in the test atmosphere Earth 1. Solar fluxes and heating
 427 rates differ by much less than 1 %. The thermal down-welling fluxes calcu-
 428 lated by RRTM and MRAC show large differences in the stratosphere below
 429 pressures of around 10^{-2} - 10^{-3} bar, reaching up to a factor of 5 in the upper
 430 stratosphere where pressures are below 10^{-4} bar. However, these differences
 431 are well below 1 W m^{-2} , so are not discernible on the scale in Figure 6. The
 432 up-welling fluxes differ by only about 10 % in the stratosphere, since they
 433 are dominated by the tropospheric component. Hence, the calculated resulting
 434 cooling rates differ only by small amounts of 0.1 - 0.4 K day^{-1} and usually lie
 435 within 5-10 %, especially in the upper stratosphere.

436 In order to assess the sensitivity of the model to errors in the absorption cross
 437 sections (hence, in optical depth and thermal fluxes), we artificially increased
 438 the optical depth in RRTM in the most important stratospheric band, the CO_2
 439 $15\mu\text{m}$ fundamental by factors of 2, 5, 10 and 20, respectively. Fig. 7 quantifies
 440 the effect of these sensitivity runs on the temperature profile. Fig. 7 a) shows
 441 the total optical depth calculated by RRTM and MRAC in the validation
 442 runs. Clearly, in the stratosphere, RRTM under-estimates the optical depth,
 443 as already discussed above.

444 Fig. 7 b) shows the temperature profiles for the two Earth validation runs with
 445 MRAC and RRTM, as well as for a run with RRTM, but increased optical
 446 depth by a factor of 2. This factor of 2 is representative of the error in the
 447 absorption cross section calculations in the $15 \mu\text{m}$ band due to the required
 448 extrapolation in the T - p -range, as shown in Figure 1. It can be seen that
 449 by increasing the optical depth in RRTM artificially, the temperature profile
 450 nearly reproduces the MRAC temperature profile.

451 These results show that conditions which differ too much from the Earth's
 452 standard atmosphere seem to pose problems for RRTM. This limitation was
 453 already noted in some of the previous studies performed with RRTM. Clearly,
 454 due to the use of an expanded temperature range, MRAC performs better than
 455 RRTM in these atmospheres.

456 4 About the runs

457 4.1 Absorption cross sections

458 The absorption cross sections used in the runs performed for this work (sum-
 459 marized in Tables 3 and 4) were calculated assuming a N₂-CO₂-background
 460 atmosphere, consisting of 95% molecular nitrogen and 5% carbon dioxide. Ac-
 461 cording to Kasting and Ackerman (1986) and Toth (2000), the foreign broad-
 462 ening coefficient for water is enhanced by a factor of 2 with respect to air for
 463 CO₂ as a broadening gas and by a factor of 1.2 for N₂ as a broadening gas.
 464 Similarly, for carbon dioxide the foreign broadening coefficient was enhanced
 465 by a factor of 1.3 when N₂ was the broadening gas (Kasting and Ackerman,
 466 1986). Accounting for the appropriate mixing ratios then yields an effective
 467 enhancement factor by which the foreign broadening parameter from HiTemp
 468 was multiplied before use in the cross section calculations described above.

469 We compared the calculated cross sections of the assumed N₂-CO₂-atmosphere
 470 (95% nitrogen and 5% carbon dioxide) with cross sections for some major spec-
 471 tral bands corresponding to different background atmospheres, i.e. different
 472 CO₂ concentrations. These cross sections were obtained with the line-by-line
 473 radiative transfer model Mirart (Schreier and Böttger, 2003). The cross sec-
 474 tions from the 95%-N₂-5%-CO₂-atmosphere agree within 5 % for most of the
 475 cases studied in this work, although for the runs with the lowest CO₂ concen-
 476 trations, the agreement decreased to about 10 %.

478 *4.2 Model runs*

479 There were a total number of 12 nominal runs performed as shown in Table 3.

480 We assumed a constant background pressure of 0.77 bar N_2 with variable
 481 amounts of CO_2 . Water vapour contents of the atmosphere were calculated as
 482 described in section 2.3. No other gases were present in the atmosphere, as in
 483 Kasting (1987). For several values of the solar constant ($S=0.7, 0.75, 0.8, 0.85,$
 484 0.9 and 0.95 present-day value), we increased the CO_2 partial pressure until
 485 converged surface temperatures reached 273 K (runs 1-6) and 288 K (runs 7-
 486 12), respectively. This procedure is similar to what was done by Kasting (1987).
 487 The solar constant values were chosen as to loosely correspond to important
 488 events throughout the Earth’s history, such as the beginning of the main se-
 489 quence life time of the Sun ($S=0.70$, 4.6 Gy ago), the end of the late heavy
 490 bombardment ($S=0.75$, 3.8 Gy ago), the rise of oxygenesis by cyanobacteria
 491 ($S=0.80$, 2.9 Gy ago), the first and the second oxidation event ($S=0.85$ and
 492 $S=0.90$, 2 and 1.3 Gy ago respectively) and the Cambrian explosion ($S=0.95$,
 493 0.6 Gy ago). Assigning geological ages to the solar constants used in the model
 494 (see Table 3) is essential when comparing the calculated model CO_2 concentra-
 495 tions to the available data and constraints on carbon dioxide. In this work, we
 496 chose two approximations of the solar luminosity $S(t)$ with time. The first one
 497 is from Caldeira and Kasting (1992), the second approximation is from Gough
 498 (1981). The difference of these two formulations is most pronounced for earlier
 499 time periods before 1-2 Gy ago, although it is rarely larger than a few percent.

500 The total surface pressure is always calculated from the relation $p_{\text{surf}} = p_{\text{CO}_2} +$
 501 $p_{\text{N}_2} + p_{\text{H}_2\text{O}}$. Since we calculated surface temperatures of 273 K and 288 K,
 502 the amount of surface pressure which arose from the evaporation of water is
 503 about 6 mb and 17 mb, respectively. Note that the total surface pressure in

our model runs decreases with time, as we assume less CO₂ partial pressure in our model atmospheres. There is no geological data available on the total surface pressure throughout time, however, our approach of constant N₂ partial pressure is consistent with assumptions made in previous studies (e.g., Kasting, 1987).

4.3 *Parameter variations of surface albedo and relative humidity profile*

Previous works regarding the "faint young Sun problem" have concentrated on the increased greenhouse effect, as stated above in the Introduction. We also studied two important parameters affecting the surface temperature in our model, namely the surface albedo and the relative humidity (RH) distribution.

The importance of cloud coverage for the surface temperature, e.g. on early Mars, has been studied by Mischna et al. (2000). The effect in their model was quite large, yielding surface temperatures from 220 K to 290 K, depending on cloud optical depth and cloud location. In our model, the surface albedo simulates the presence of clouds, as stated above in the description of our model.

Water vapour is a very effective greenhouse gas. In contrast to CO₂, its content in the troposphere (where 99 % of the column resides) is controlled by the hydrological cycle (ocean reservoir, evaporation, subsequent condensation and precipitation) which is very sensitive to temperature. A critical parameter in climate models is the relative humidity parametrization, which clearly has a potentially large impact on the water content in the atmosphere and hence on the resulting greenhouse effect.

In addition to the model runs described above, we therefore performed runs varying surface albedo and relative humidity profiles. These runs are based on runs 3 and 4 of Table 3, i.e. solar constants of $S=0.8$ and $S=0.85$. Table 4 summarizes the parameter variations.

531 In the runs from Table 3, the surface albedo is normally set to $A=0.21$ (see
 532 Table 2). Now, we assume surface albedos of $A \pm 10\%$, i.e. 0.19 and 0.23,
 533 respectively.

534 The relative humidity profile used for the calculation of water vapour con-
 535 centrations in Table 3 follows the approach of Manabe and Wetherald (1967)
 536 (referred to as RH=MW, see section 2.3). Here, for the additional parameter
 537 studies, we used three different RH profiles. The first one assumed a saturated
 538 troposphere (RH=1). The second profile used RH=0, i.e. water was removed
 539 from the atmosphere. These two profiles represent the lower and upper lim-
 540 its of the atmospheric water content. The third RH profile is a more realis-
 541 tic RH profile. It is based on a temperature correction to the RH profile of
 542 Manabe and Wetherald (1967) which was first proposed by Cess (1976) and
 543 later used by Vardavas and Carver (1985).:

$$R = R_{\text{surface}} \cdot R_{\text{mw}}^{1-0.03(T_S-288)} \quad (23)$$

544 where $R_{\text{surface}} \cdot R_{\text{mw}}$ is the relative humidity distribution from eq. 22. This
 545 profile is referred to as RH=C. Figure 8 shows the difference between the
 546 two RH profiles from Manabe and Wetherald (1967) and Vardavas and Carver
 547 (1985). The total amount of water vapour is reduced by about 20 % by us-
 548 ing the temperature correction of Vardavas and Carver (1985) compared to
 549 Manabe and Wetherald (1967).

550 5 Results and Discussion

551 5.1 Examples of thermal structure and water profiles

552 Figure 9 shows the temperature profiles for run 3 (plain line) and run 4 (dotted
 553 line). Run 3 ($S = 0.80$) considered 20 mb CO₂ partial pressure, run 4 ($S =$

0.85) roughly 3 mb (see Table 3). These two runs were chosen because they represent interesting points in time, such as the advent of cyanobacteria (run 3) and the first oxidation event (run 4).

Clearly, in the troposphere the temperature differences for the two runs are rather small. In the lower to middle stratosphere (from around 10 to 25 km), run 4 (dashed line) shows lower temperatures than run 3 (plain line). In this region, absorption of solar radiation by CO_2 is the dominant heating process, eventually causing a temperature inversion from the middle stratosphere upwards (seen for both runs in Fig. 9 for higher altitudes above 25-30 km). In the upper stratosphere (above 25-30 km), where CO_2 radiative cooling via the $15\ \mu\text{m}$ fundamental band sets in, run 3 shows lower temperatures than run 4. This reflects the lower flux and higher CO_2 concentrations in run 3 compared to run 4.

However, as already noted by Segura et al. (2003), the actual strength of the temperature inversion is not well determined due to less accurate transmittance calculations in the solar code and may well turn out to be a mere numerical problem rather than reflecting physical processes.

Also indicated in Fig. 9 are the convective zones for both runs. The convective zone for the $S = 0.8$ case only reaches up to about 3 km altitude, whereas in the $S = 0.85$ case, it extends already to about 7.5 km, which is closer to the present-day, latitude-dependent value of 10-20 km. However, the lapse rate remains close to the adiabatic value for several kilometres after entering the regime of radiative equilibrium (above the dot-dashed lines in Fig. 9).

Figure 10 is similar to Fig. 9, but it shows the resulting water profiles. There is considerably less water in the stratosphere for the $S = 0.85$ case due to enhanced condensation. The cold trap position is indicated, as well as the tropopause position, i.e. the boundary between the convective and non-convective regime.

582 Figures 9 and 10 illustrate some interesting features regarding the thermal
 583 structure of the atmosphere. The cold trap, i.e. the highest point up to which
 584 water is allowed to condense out in the model, is no longer located near the
 585 tropopause, as is the case in the atmosphere of modern Earth. It is still as-
 586 sociated with a temperature inversion, but as this inversion occurs at higher
 587 altitudes, cold trap and tropopause (i.e., the boundary between convective and
 588 non-convective layers) are located at noticeably different altitudes. It seems
 589 that the observation that tropopause, cold trap and temperature inversion oc-
 590 cur at approximately the same height in the modern Earth's atmosphere is
 591 somewhat coincidental.

592 5.2 Climatic constraints on CO_2 partial pressures

593 The results of the 12 nominal runs (see Table 4) are summarized in Fig. 11. The
 594 lower plain line indicates the CO_2 partial pressures corresponding to calculated
 595 surface temperatures of 273 K (runs 1-6), the upper plain line shows the partial
 596 pressures for surface temperatures of 288 K (runs 7-12). For comparison, the
 597 dashed line shows the partial pressures as calculated by Kasting (1987). Fig. 11
 598 shows that our new radiative scheme requires considerably less CO_2 (about a
 599 factor of 2-15) to achieve an ice-free surface than the study of Kasting (1987).

600 Note that the radiative transfer scheme used by Kasting (1987) was applicable
 601 to this type of atmospheres, as is the one we used.

602 Also indicated in Fig. 11 are the upper limits of CO_2 partial pressures as
 603 inferred from sedimentary data.

604 Several attempts have been made to constrain the CO_2 content of the early
 605 Earth atmosphere. For example, among others, Rye et al. (1995), Hessler et al.
 606 (2004) and Towe (1985) have placed upper limits on CO_2 partial pressures dur-
 607 ing different periods of the mid-Archaean to early Proterozoic of approximately
 608 10-100 PAL (Present Atmospheric Level), depending on temperature. These

limits were based on experimental sediment data and on biological consid-
erations. Rye et al. (1995) and Hessler et al. (2004) argued for upper limits
on CO₂ partial pressures based on the observations that in ancient Archaean
rocks, siderites are missing. Towe (1985) stated atmospheric upper levels of
CO₂ based on the observation that anaerobic photosynthesis and nitrogen fix-
ation (which are both believed to be evolutionary ancient) are incompatible
with high CO₂ concentrations.

Previous climate studies of the early Earth's atmosphere calculated very high
CO₂ partial pressures in order to raise the surface temperature above 273 K.
The model CO₂ values were generally above 50 mb well into Proterozoic age
(e.g., Kasting 1987, see also Fig. 11). However, the experimental data from
sediments and biology (see above) were of the order of several mb, i.e. an
order of magnitude lower. This contradiction is known as the "faint young Sun
problem".

Fig. 11 however shows that for the late Archaean (solar constant $S=0.85$), our
new results are compatible with the paleosol records, hence the "faint young
Sun problem" might be resolved for this time period.

One should note that the absence of methane, ozone, ammonia or other green-
house gases in our results implies that we calculated only a lower limit for
surface temperatures. Photochemical models of the anoxic Archaean and low-
oxygen Proterozoic atmospheres have shown that methane could build up to
concentrations of the order of 10^{-3} (Pavlov et al., 2003) which could also have
contributed to the greenhouse effect. Haqq-Misra et al. (2008) proposed higher
hydrocarbons such as C₂H₆ in a methane-rich atmosphere as radiative gases.
Those effects were not investigated here. Our studies imply, however, that
much less to none additional greenhouse gases are required to warm the early
Earth.

636 *5.2.1 Effect of parameter variations of surface albedo and relative humidity*

637 Table 4 summarizes the results of the parameter variations. Shown are the val-
638 ues of CO₂ partial pressure required to obtain the desired surface temperature
639 of 273 K.

640 Upon lowering the surface albedo value from 0.23 to 0.19, the partial pressure
641 of CO₂ required to keep the surface at 273 K is reduced from 28.5 mb to 11.0
642 mb (at $S=0.80$) and from 5.5 mb to 1.5 mb (at $S=0.85$). This is a lowering of
643 the amount of CO₂ by factors of 2.6 and 3.7, respectively.

644 When changing the RH profile from saturated (RH=1) to water-free condi-
645 tions (RH=0), the necessary partial pressure of CO₂ has to be increased from
646 4.9 mb to 266.8 mb ($S=0.80$) and from 0.6 mb to 180.6 mb ($S=0.85$). How-
647 ever, like expected, the comparison between the more realistic RH profiles
648 of Manabe and Wetherald (1967) and Cess (1976) yields much smaller differ-
649 ences. When changing the RH profile from RH=MW to RH=C, CO₂ partial
650 pressures must be increased from 19.1 mb to 27.3 mb ($S=0.80$) and from 2.9
651 mb to 4.9 mb ($S=0.85$). These differences amount to 43 % and 69 %, respec-
652 tively, which is much lower than the differences obtained by varying the surface
653 albedo.

654 These parameter variations demonstrated that the surface albedo, hence clouds,
655 is a very important parameter in view of the surface temperature. The results
656 obtained imply that the latter is probably more important than the RH profile,
657 although the RH profile has to be incorporated more consistently to accurately
658 constrain CO₂ partial pressures for the "faint young Sun" problem. This calls
659 for a more elaborated 1D model incorporating clouds and cloud formation as
660 was done by, e.g., Colaprete and Toon (2003) for early Mars. In the future, we
661 plan to add clouds to our code.

662 The results of the parameter variations, however, did not significantly change
663 our main conclusion, namely that the CO₂ values for the late Archaean cal-

culated by our improved model are consistent with observational data. The CO_2 values obtained for the parameter variations range between 1.5-5.5 mb of partial pressure. This is still close to the values inferred from the paleosol record.

6 Summary

In this work, we addressed the "faint young Sun problem" of the ice-free early Earth. In order to do this, we applied a one-dimensional radiative-convective model to the atmosphere of the early Earth. Our model included updated absorption coefficients in the thermal radiative transfer scheme.

The validations done for the new radiative transfer scheme have been described. The new scheme is found to perform significantly better than a previous scheme under conditions deviating from the modern Earth atmosphere.

We then studied the effect of enhanced carbon dioxide concentrations and parameter variations of the surface albedo and the relative humidity profiles on the surface temperature of the early Earth with the improved model.

Our new model simulations suggest that the amount of CO_2 needed to keep the surface of the early Earth from freezing is significantly less (up to an order of magnitude) than previously thought (see Figure 11).

For the late Archaean and early Proterozoic period (around 2-2.5 Gy ago), the calculated amount of CO_2 (2.9 mb partial pressure) which is needed to obtain a surface temperature of 273 K is compatible with the amount inferred from geological data, contrary to previous studies (see Figure 11). The apparent contradiction between model constraints on CO_2 and sediment data disappears for this time period.

Upon varying model parameters such as the surface albedo and relative hu-

689 midity profile, we found this conclusion to be robust. The calculated CO₂
690 partial pressures for the late Archaean (1.5-5.5 mb) are still consistent with
691 the geological evidence.

692 **Acknowledgements**

693 We are grateful to Jim Kasting and Eli Mlawer for useful discussion while cre-
694 ating the new radiation scheme. Furthermore, we are grateful to Viola Vogler
695 for help in doing some of the plots in this paper.

696 We thank the two anonymous referees for their constructive remarks which
697 helped to improve and clarify this paper.

698 **References**

- 699 Brown, L. R., Benner, C., Devi, V. M., Smith, M. A. H., Toth, R. A., 2005.
700 Line mixing in self- and foreign-broadened water vapor at 6 μm . *Journal of*
701 *Molecular Structure* 742, 111122.
- 702 Caldeira, K., Kasting, J. F., Dec. 1992. The life span of the biosphere revisited.
703 *Nature* 360, 721–723.
- 704 Cess, R. D., 1976. Climatic change: An appraisal of atmospheric feedback
705 mechanisms employing zonal climatology. *J. Atmospheric Sciences* 33, 1831–
706 1843.
- 707 Colaprete, A., Toon, O. B., Apr. 2003. Carbon dioxide clouds in an early dense
708 Martian atmosphere. *Journal of Geophysical Research (Planets)* 108, 5025.
- 709 Goody, R., West, R., Chen, L., Crisp, D., Dec. 1989. The correlated-k method
710 for radiation calculations in nonhomogeneous atmospheres. *J. Quant. Spec-*
711 *troscopy and Radiative Transfer* 42, 539–550.
- 712 Goody, R. M., Yung, Y. L., 1989. *Atmospheric radiation: Theoretical basis.*
713 2nd ed., New York, NY: Oxford University Press.
- 714 Gough, D. O., Nov. 1981. Solar interior structure and luminosity variations.
715 *Solar Physics* 74, 21–34.
- 716 Grenfell, J. L., Griebmeier, J.-M., Patzer, B., Rauer, H., Segura, A., Stadel-
717 mann, A., Stracke, B., Titz, R., Von Paris, P., Feb. 2007a. Biomarker Re-
718 sponse to Galactic Cosmic Ray-Induced NO_x and the Methane Greenhouse
719 Effect in the Atmosphere of an Earth-Like Planet Orbiting an M Dwarf Star.
720 *Astrobiology* 7, 208–221.
- 721 Grenfell, J. L., Stracke, B., von Paris, P., Patzer, B., Titz, R., Segura, A.,
722 Rauer, H., Apr. 2007b. The response of atmospheric chemistry on earthlike
723 planets around F, G and K Stars to small variations in orbital distance.
724 *Planetary and Space Science* 55, 661–671.
- 725 Haqq-Misra, J., Domagal-Goldman, S., Kasting, P., Kasting, J. F., 2008. A
726 Revised, Hazy Methane Greenhouse for the Archaean Earth. accepted in
727 *Astrobiology*.

Hessler, A., Lowe, D., Jones, R., Bird, D., Apr. 2004. A lower limit for atmospheric carbon dioxide levels 3.2 billion years ago. *Nature* 428, 736–738.

Ingersoll, A. P., Nov. 1969. The Runaway Greenhouse: A History of Water on Venus. *J. Atmospheric Sciences* 26, 1191–1198.

Jenkins, G. S., 2000. Global climate model high-obliquity solutions to the ancient climate puzzles of the Faint-Young Sun Paradox and low-latitude Proterozoic Glaciation. *J. Geophys. Res.* 105, 7357–7370.

Kasting, J. F., Feb. 1987. Theoretical constraints on oxygen and carbon dioxide concentrations in the Precambrian atmosphere. *Precambrian Research* 34, 205–229.

Kasting, J. F., Jun. 1988. Runaway and moist greenhouse atmospheres and the evolution of earth and Venus. *Icarus* 74, 472–494.

Kasting, J. F., Ackerman, T. P., Dec. 1986. Climatic consequences of very high carbon dioxide levels in the Earth’s early atmosphere. *Science* 234, 1383–1385.

Kasting, J. F., Howard, M. T., 2006. Atmospheric composition and climate on the early Earth. *Phil. Trans. R. Soc. B* 361, 1733–1742.

Kasting, J. F., Pollack, J. B., Ackerman, T. P., Mar. 1984a. Response of earth’s atmosphere to increases in solar flux and implications for loss of water from Venus. *Icarus* 57, 335–355.

Kasting, J. F., Pollack, J. B., Crisp, D., 1984b. Effects of high CO₂ levels on surface temperature and atmospheric oxidation state of the early Earth. *J. Atmospheric Chemistry* 1, 403–428.

Kasting, J. F., Whitmire, D. P., Reynolds, R. T., Jan. 1993. Habitable Zones around Main Sequence Stars. *Icarus* 101, 108–128.

Knauth, P., Lowe, D. R., 2003. High Archean climatic temperature inferred from oxygen isotope geochemistry of cherts in the 3.5 Ga Swaziland Supergroup, South Africa. *GSA Bull.* 115, 566–580.

Lacis, A. A., Oinas, V., May 1991. A description of the correlated-k distribution method for modelling nongray gaseous absorption, thermal emission, and multiple scattering in vertically inhomogeneous atmospheres. *J. Geophys.*

759 Res. 96, 9027–9064.

760 Manabe, S., Wetherald, R. T., May 1967. Thermal Equilibrium of the At-
761 mosphere with a Given Distribution of Relative Humidity. *J. Atmospheric*
762 *Sciences* 24, 241–259.

763 Minton, D. A., Malhotra, R., May 2007. Assessing the Massive Young Sun
764 Hypothesis to Solve the Warm Young Earth Puzzle. *Astrophysical Journal*
765 660, 1700–1706.

766 Mischna, M. A., Kasting, J. F., Pavlov, A., Freedman, R., Jun. 2000. Influence
767 of carbon dioxide clouds on early martian climate. *Icarus* 145, 546–554.

768 Mlawer, E. J., Taubman, S. J., Brown, P. D., Iacono, M. J., Clough, S. A., Jul.
769 1997. Radiative transfer for inhomogeneous atmospheres: RRTM, a validated
770 correlated-k model for the longwave. *J. Geophys. Res.* 102, 16663–16682.

771 Mojzsis, S. J., Arrhenius, G., McKeegan, K. D., Harrison, T. M., Nutman,
772 A. P., Friend, C. R. L., Nov. 1996. Evidence for life on Earth before 3,800
773 million years ago. *Nature* 384, 55–59.

774 Pavlov, A. A., Brown, L. L., Kasting, J. F., Oct. 2001. UV shielding of NH₃
775 and O₂ by organic hazes in the Archean atmosphere. *J. Geophys. Res.* 106,
776 23267–23288.

777 Pavlov, A. A., Hurtgen, M. T., Kasting, J. F., Arthur, M. A., Jan. 2003.
778 Methane-rich Proterozoic atmosphere? *Geology* 31, 87–90.

779 Pavlov, A. A., Kasting, J. F., Brown, L. L., Rages, K. A., Freedman, R., May
780 2000. Greenhouse warming by CH₄ in the atmosphere of early Earth. *J.*
781 *Geophys. Res.* 105, 11981–11990.

782 Robert, F., Chaussidon, M., Oct. 2006. A palaeotemperature curve for the
783 Precambrian oceans based on silicon isotopes in cherts . *Nature* 443, 969–
784 972.

785 Rosing, M. T., Frei, R., Jan. 2004. U-rich Archean sea-floor sediments from
786 Greenland - indications of >3700 Ma oxygenic photosynthesis. *Earth and*
787 *Planetary Science Letters* 217, 237–244.

788 Rothman, L. S., Gamache, R. R., Tipping, R. H., Rinsland, C. P., Smith,
789 M. A. H., Benner, D. C., Devi, V. M., Flaud, J.-M., Camy-Peyret, C., Perrin,

790 A., 1992. The HITRAN molecular data base - Editions of 1991 and 1992. J.
791 Quant. Spectroscopy and Radiative Transfer 48, 469–507.

792 Rothman, L. S., Wattson, R. B., Gamache, R., Schroeder, J. W., McCann,
793 A., Jun. 1995. HITRAN HAWKS and HITEMP: high-temperature molec-
794 ular database. In: Dainty, J. C. (Ed.), Proc. SPIE Vol. 2471, p. 105–111,
795 Atmospheric Propagation and Remote Sensing IV. Presented at the Society
796 of Photo-Optical Instrumentation Engineers (SPIE) Conference.

797 Rye, R., Kuo, P. H., Holland, H. D., Dec. 1995. Atmospheric carbon dioxide
798 concentrations before 2.2 billion years ago. Nature 378, 603–605.

799 Sagan, C., Chyba, C., 1997. The early faint sun paradox: Organic shielding of
800 ultraviolet-labile greenhouse gases. Science 276, 1217–1221.

801 Sagan, C., Mullen, G., Jul. 1972. Earth and Mars: Evolution of Atmospheres
802 and Surface Temperatures. Science 177, 52–56.

803 Schreier, F., Böttger, U., 2003. MIRART, a line-by-line code for infrared at-
804 mospheric radiation computations including derivatives. Atmospheric and
805 Oceanic Optics 16, 262–268.

806 Segura, A., Kasting, J. F., Meadows, V., Cohen, M., Scalo, J., Crisp, D., Butler,
807 R. A. H., Tinetti, G., Dec. 2005. Biosignatures from Earth-Like Planets
808 Around M Dwarfs. Astrobiology 5, 706–725.

809 Segura, A., Krelove, K., Kasting, J. F., Sommerlatt, D., Meadows, V., Crisp,
810 D., Cohen, M., Mlawer, E., Dec. 2003. Ozone Concentrations and Ultraviolet
811 Fluxes on Earth-Like Planets Around Other Stars. Astrobiology 3, 689–708.

812 Shaviv, N. J., Dec. 2003. Toward a solution to the early faint Sun paradox: A
813 lower cosmic ray flux from a stronger solar wind. J. Geophys. Res. (Space
814 Physics) 108, 1437.

815 Shields, G. A., Kasting, J. F., 2007. Palaeoclimatology: Evidence for hot early
816 oceans? Nature 447, E1.

817 Sleep, N. H., Hessler, A. M., Jan. 2006. Weathering of quartz as an Archean
818 climatic indicator. Earth and Planetary Science Letters 241, 594–602.

819 Toon, O. B., McKay, C. P., Ackerman, T. P., Santhanam, K., 1989. Rapid
820 calculation of radiative heating rates and photodissociation rates in inhomo-

821 geneous multiple scattering atmospheres. J. Geophys. Res. 94, 16287–16301.
 822 Toth, R., 2000. Air- and N₂-Broadening Parameters of Water Vapor: 604 to
 823 2271 cm⁻¹. J. Molec. Spectroscopy 201, 218–243.
 824 Towe, K., 1985. Habitability of the Early Earth - Clues from the Physiology
 825 of Nitrogen Fixation and Photosynthesis. Origins of Life 15, 235–250.
 826 Vardavas, I. M., Carver, J. H., Oct. 1984. Solar and terrestrial parameter-
 827 izations for radiative-convective models. Planetary and Space Science 32,
 828 1307–1325.
 829 Vardavas, I. M., Carver, J. H., Oct. 1985. Atmospheric temperature response
 830 to variations in CO₂ concentration and the solar-constant. Planetary and
 831 Space Science 33, 1187–1207.
 832 West, R., Crisp, D., Chen, L., Mar. 1990. Mapping transformations for broad-
 833 band atmospheric radiation calculations. J. Quant. Spectroscopy and Ra-
 834 diative Transfer 43, 191–199.
 835 Wiscombe, W. J., Evans, J., 1977. Exponential-sum fitting of radiative trans-
 836 mission functions. Journal of Computational Physics 24, 416–444.

837 **Figure captions**

838 Figure 1:

839 Range of T - p values used to obtain absorption cross sections in the two radia-
840 tive schemes RRTM (light grey) and MRAC (dark grey).

841

842 Figure 2:

843 Cumulative k distribution for parts of the $6.3\ \mu\text{m}$ H_2O fundamental band,
844 $T=240\ \text{K}$ and $p=10\ \text{mb}$: Comparison between Lacis and Oinas (1991) (plain
845 line) and our algorithm (dotted).

846

847 Figure 3:

848 Cumulative k distribution for parts of the $15\ \mu\text{m}$ CO_2 fundamental band
849 between 630 and $700\ \text{cm}^{-1}$, $T=260\ \text{K}$ and $p=507\ \text{mb}$: Comparison between
850 Mlawer et al. (1997) (plain line) and our algorithm (dotted).

851

852 Figure 4:

853 Comparison of validation temperature profiles (RRTM plain line, MRAC dot-
854 ted line).

855

856 Figure 5:

857 Limits of the RRTM temperature grid. Atmospheric conditions as for the stan-
858 dard CO_2 case in fig. 4, RRTM profile (plain), MRAC (dotted). The shaded
859 area designates the validity range of RRTM as already indicated in fig. 1.

860

861 Figure 6:

862 Flux profiles (thermal and solar up- and down-welling fluxes) (left panel) and
863 heating and cooling rates (right panel) calculated by the two radiative schemes
864 in the test atmosphere.

865

866 Figure 7:

867 Effect of variations in the optical depth on the temperature profile calculated
868 by RRTM: Left panel, total optical depth, right panel, temperature profiles.

869

870 Figure 8:

871 Differences of the two relative humidity profiles used for the parameter varia-
872 tions

873

874 Figure 9:

875 Temperature profiles for runs with solar constants of $S = 0.8$ (run 3, plain
876 line) and $S = 0.85$ (run 4, dotted); the background pressure is 0.77 bar of N_2 .
877 The convective zones are indicated for both runs.

878

879 Figure 10:

880 Water profiles for runs with solar constants of $S = 0.8$ (run 3, plain line) and
881 $S = 0.85$ (run 4, dashed); the background pressure is 0.77 bar of N_2 . Cold trap
882 positions and tropopause positions are indicated for both runs.

883

884 Figure 11:

885 Minimal values of CO_2 partial pressure required to obtain chosen surface tem-

886 peratures of 273 K and 288 K at a fixed N_2 partial pressure for different solar
887 constants: shown are the curves for the new model (plain lines, upper line
888 288 K, lower line 273 K) and the model of Kasting (1987) (dashed)). Symbols
889 are included which represent the upper CO_2 limits derived from the sediment
890 record (\square : age conversion by Caldeira and Kasting (1992), \triangle : age conversion
891 by Gough (1981)).

Table 1

Contribution of model species to the temperature profile via radiative transfer for solar or thermal radiation, adiabatic lapse rate formulations or heat capacity contributions (x: active species, -: inactive species)

| Gas | Solar | Rayleigh | Thermal | Continuum | Lapse Rate | Heat Cap. |
|------------------|-------|----------|---------|-----------|------------|-----------|
| N ₂ | - | x | - | - | - | x |
| H ₂ O | x | - | x | x | x | - |
| O ₂ | - | x | - | - | - | x |
| Ar | - | - | - | - | - | x |
| CO ₂ | x | x | x | x | - | x |
| CO | - | - | x | - | - | x |

Table 2

Initial values, boundary conditions and parameters in the model (IV: initial value, BC: boundary condition, P: parameter)

| Quantity | Value | Type |
|-------------------|-------------------------|------|
| T_0 -profile | US Standard 1976 | IV |
| TOA incident flux | solar spectrum | BC |
| TOA p_0 | $6.6 \cdot 10^{-5}$ bar | P |
| Surface albedo | 0.21 | P |
| Zenith angle | 60° | P |

Table 3

Summary of model runs performed for this work (partial pressures p_{N_2} and p_{CO_2} and surface pressure p_{surf} are in mb, surface temperature T_{surf} in K)

| Runs | solar constant S | p_{surf} | p_{CO_2} | p_{N_2} | T_{surf} |
|------|--------------------|-------------------|-------------------|------------------|-------------------|
| 1 | 0.70 | 911 | 135.3 | 770 | 273 |
| 2 | 0.75 | 833 | 57.2 | 770 | 273 |
| 3 | 0.80 | 795 | 19.1 | 770 | 273 |
| 4 | 0.85 | 779 | 2.9 | 770 | 273 |
| 5 | 0.90 | 776 | 0.3 | 770 | 273 |
| 6 | 0.95 | 776 | 0.03 | 770 | 273 |
| 7 | 0.70 | 1192 | 405.6 | 770 | 288 |
| 8 | 0.75 | 1055 | 268.1 | 770 | 288 |
| 9 | 0.80 | 942 | 155.0 | 770 | 288 |
| 10 | 0.85 | 863 | 76.2 | 770 | 288 |
| 11 | 0.90 | 820 | 33.1 | 770 | 288 |
| 12 | 0.95 | 797 | 9.8 | 770 | 288 |

Table 4

Summary of sensitivity runs performed (RH profiles: MW Manabe and Wetherald (1967), C Cess (1976)). Partial CO₂ pressure p_{CO_2} to reach 273 K in mb.

| Run number | solar constant S | RH profile | Surface albedo | T_{surf} | p_{CO_2} |
|------------|--------------------|------------|----------------|-------------------|-------------------|
| 1a | 0.80 | MW | 0.19 | 273 | 11.0 |
| 2a | 0.80 | MW | 0.21 | 273 | 19.1 |
| 3a | 0.80 | MW | 0.23 | 273 | 28.5 |
| 4a | 0.85 | MW | 0.19 | 273 | 1.5 |
| 5a | 0.85 | MW | 0.21 | 273 | 2.9 |
| 6a | 0.85 | MW | 0.23 | 273 | 5.5 |
| 7a | 0.80 | MW | 0.21 | 273 | 19.1 |
| 8a | 0.80 | C | 0.21 | 273 | 27.3 |
| 9a | 0.80 | 1 | 0.21 | 273 | 4.9 |
| 10a | 0.80 | 0 | 0.21 | 273 | 266.8 |
| 11a | 0.85 | MW | 0.21 | 273 | 2.9 |
| 12a | 0.85 | C | 0.21 | 273 | 4.9 |
| 13a | 0.85 | 1 | 0.21 | 273 | 0.6 |
| 14a | 0.85 | 0 | 0.21 | 273 | 180.6 |

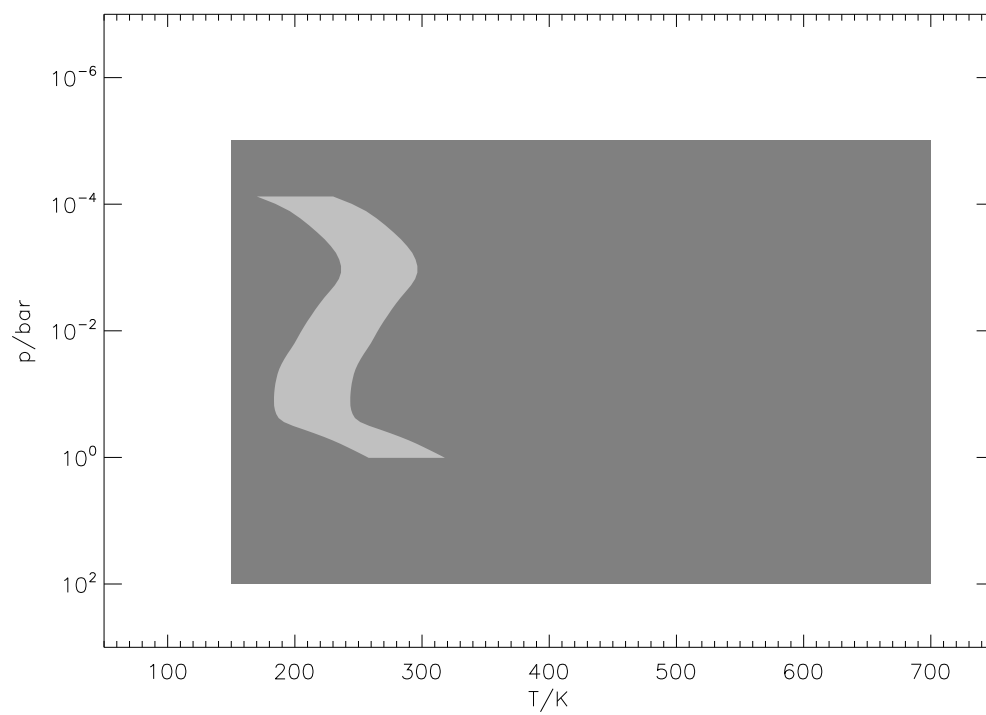


Fig. 1.

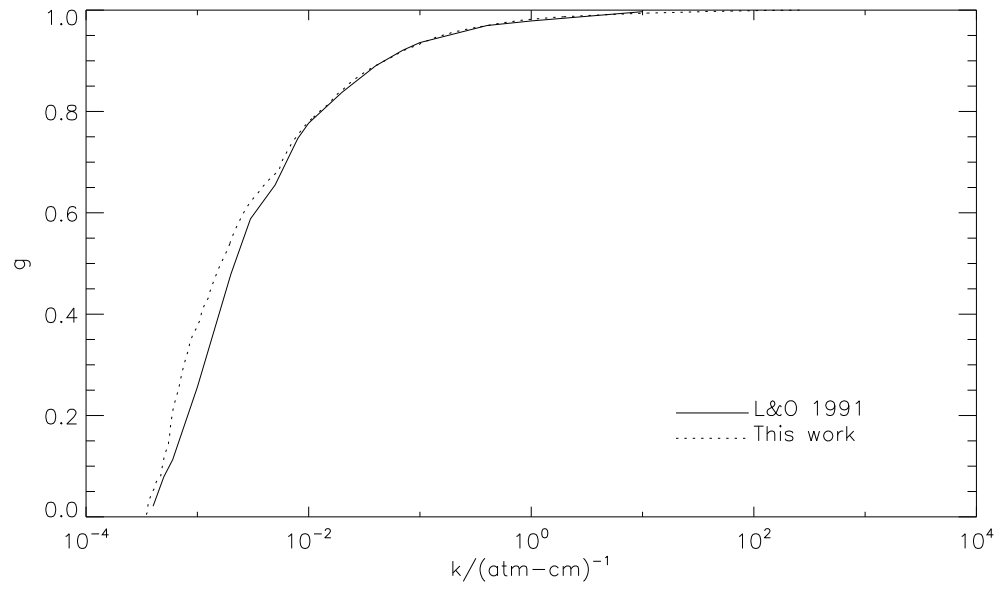


Fig. 2.

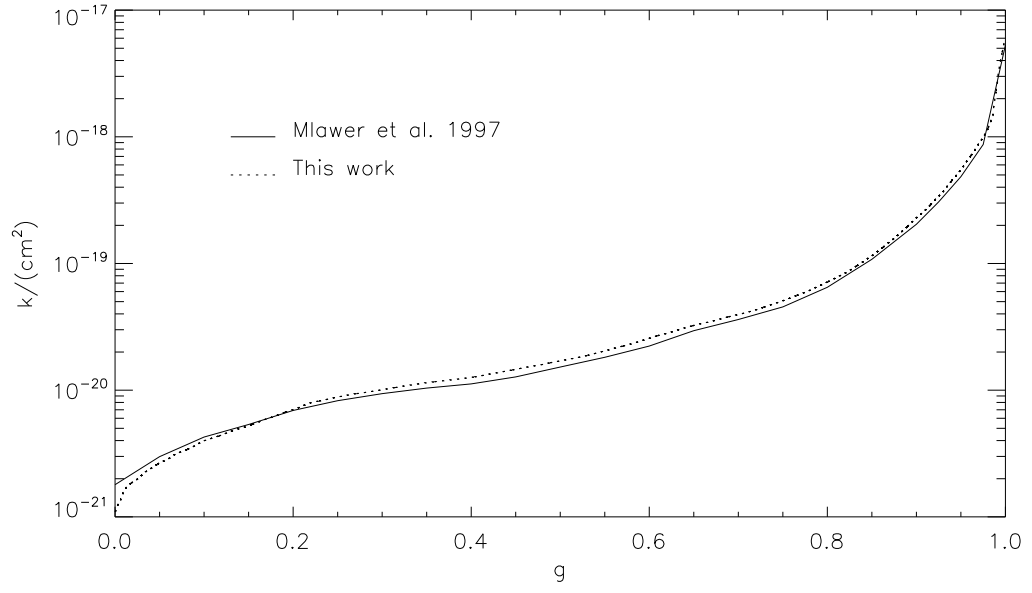


Fig. 3.

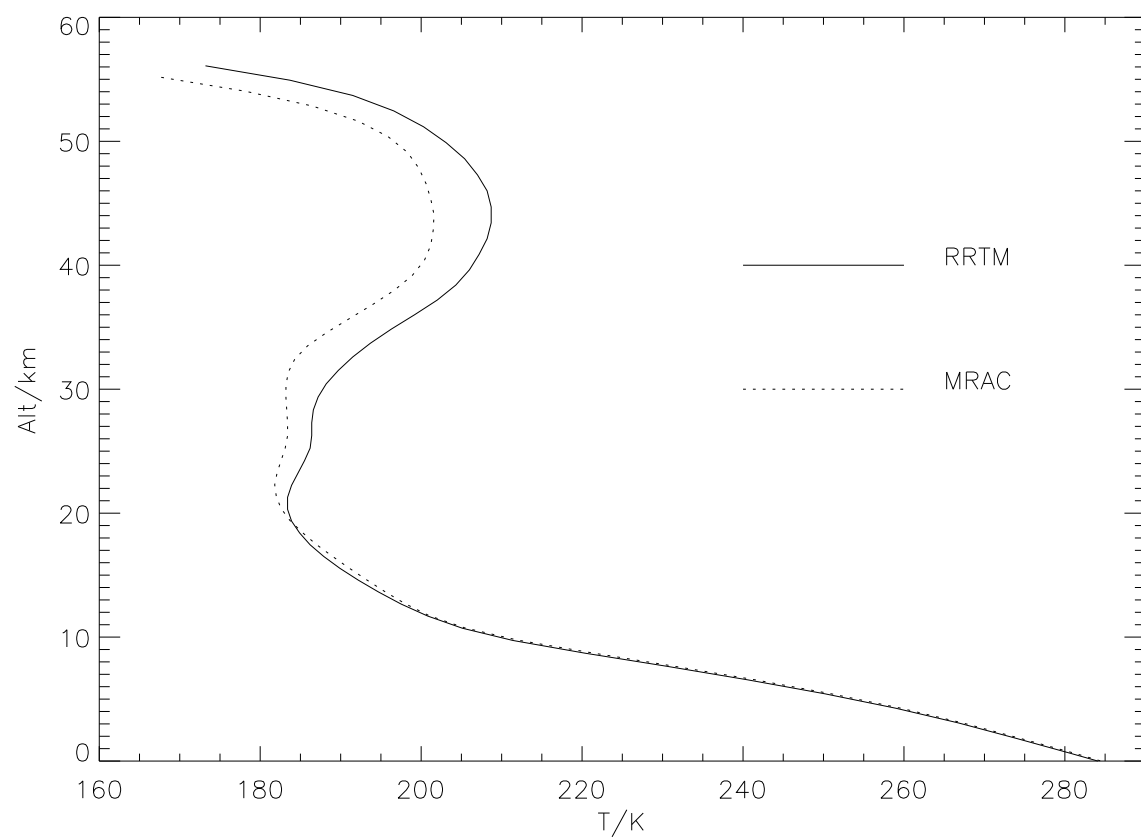


Fig. 4.

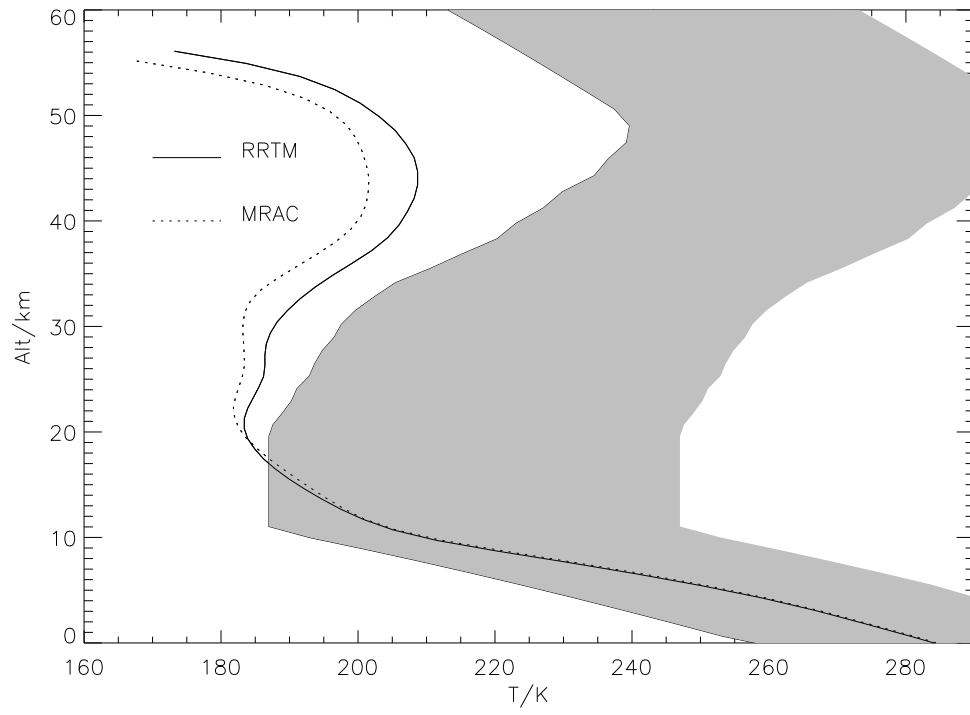


Fig. 5.

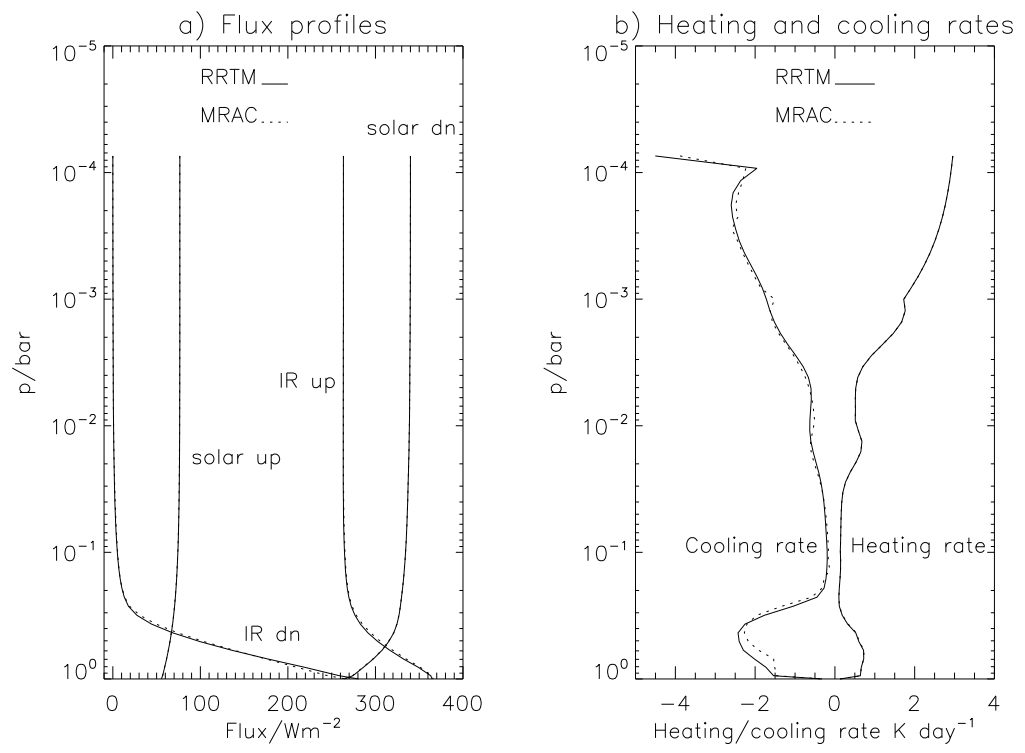


Fig. 6.

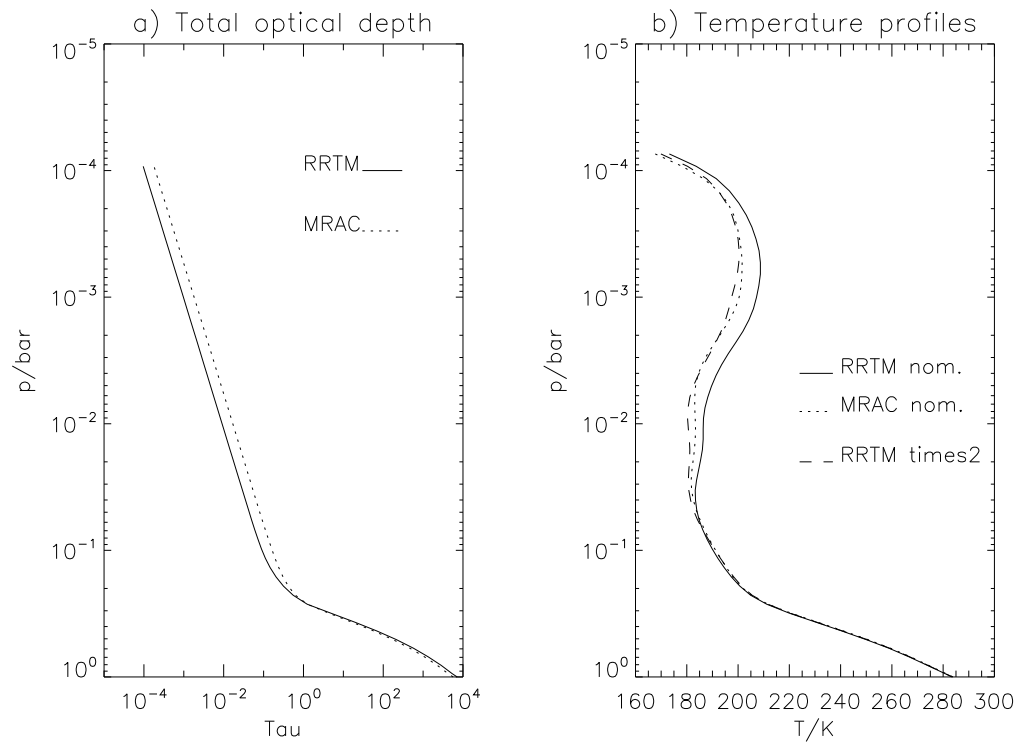


Fig. 7.

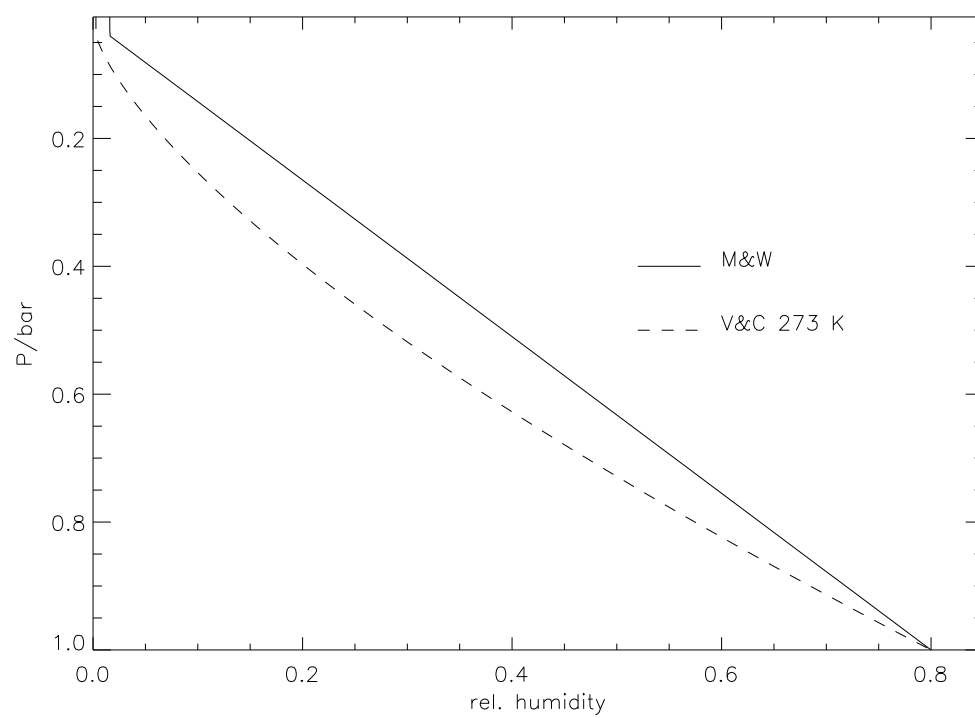


Fig. 8.

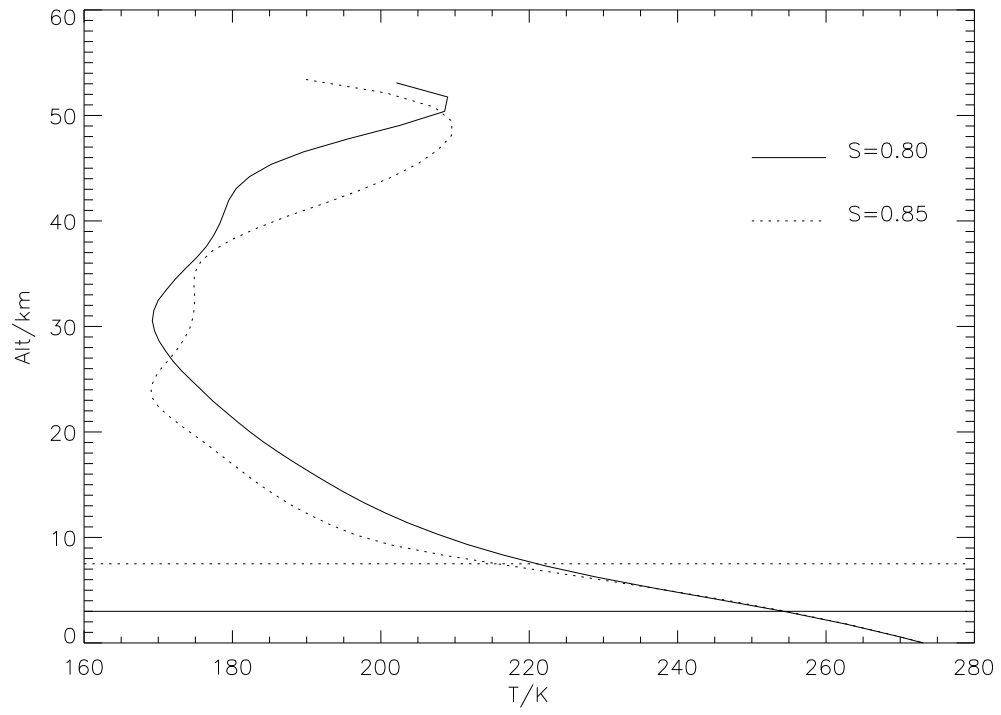


Fig. 9.

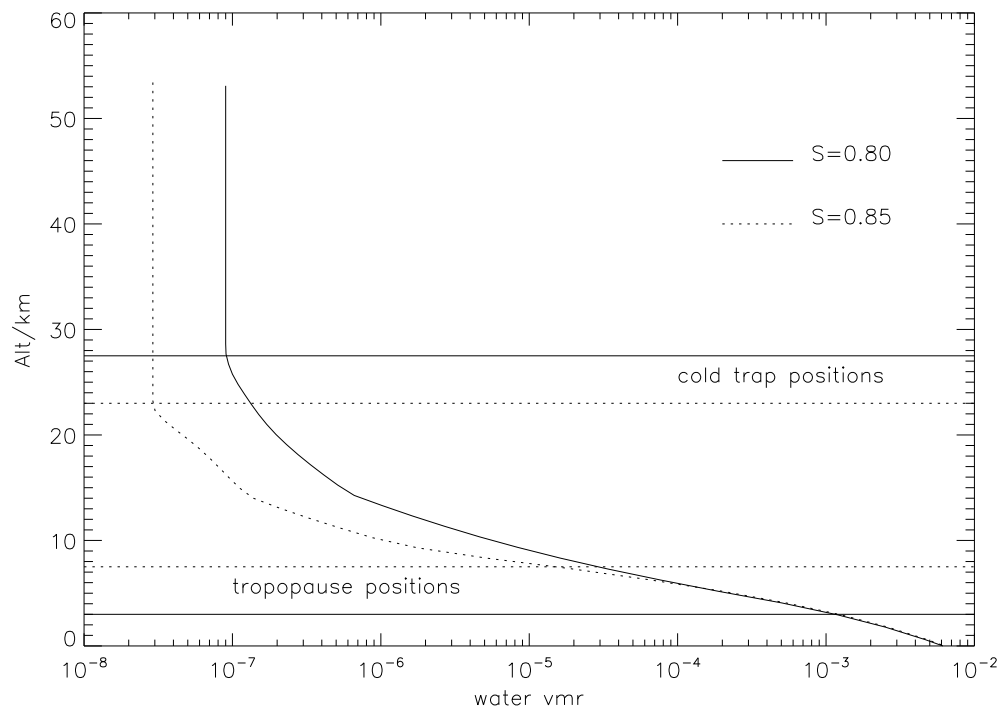


Fig. 10.

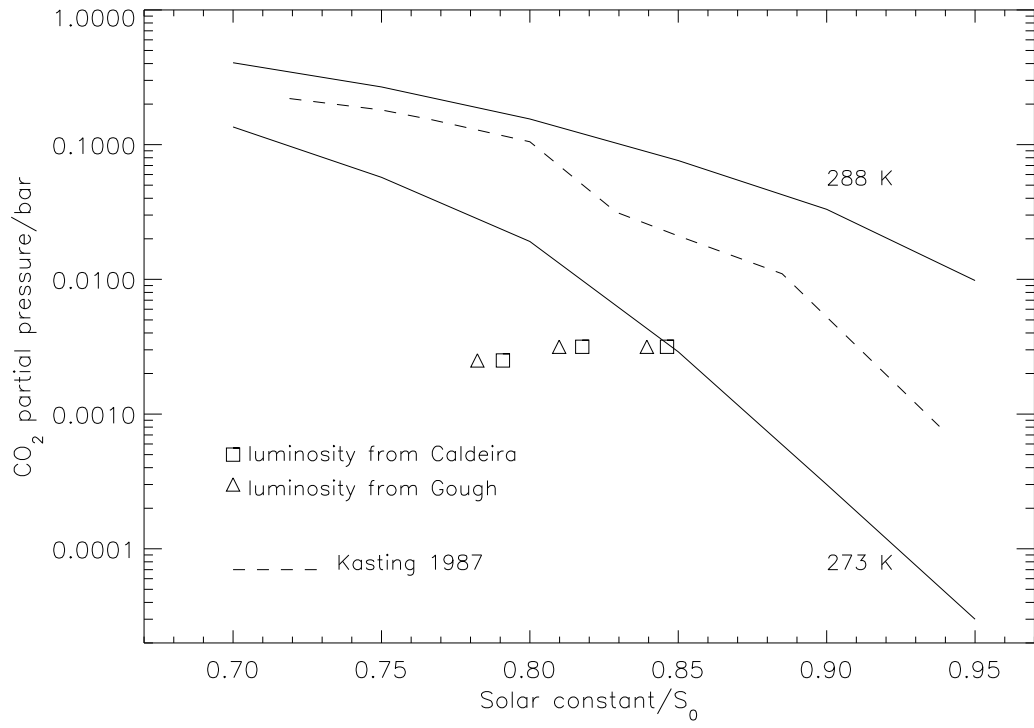


Fig. 11.